MATERIALS SCIENCE

Leaf-inspired multiresponsive MXene-based actuator for programmable smart devices

Guofa Cai[1]*, Jing-Hao Ciou[1]*, Yizhi Liu[1,2], Yi Jiang[1,3], Pooi See Lee[1†]

Natural leaves, with elaborate architectures and functional components, harvest and convert solar energy into chemical fuels that can be converted into energy based on photosynthesis. The energy produced leads to work done that inspired many autonomous systems such as light-triggered motion. On the basis of this nature-inspired phenomenon, we report an unprecedented bilayer-structured actuator based on MXene ($Ti_3C_2T_x$)–cellulose composites (MXCC) and polycarbonate membrane, which mimic not only the sophisticated leaf structure but also the energy-harvesting and conversion capabilities. The bilayer actuator features multiresponsiveness, low-power actuation, fast actuation speed, large-shape deformation, programmable adaptability, robust stability, and low-cost facile fabrication, which are highly desirable for modern soft actuator systems. We believe that these adaptive soft systems are attractive in a wide range of revolutionary technologies such as soft robots, smart switch, information encryption, infrared dynamic display, camouflage, and temperature regulation, as well as human-machine interface such as haptics.

INTRODUCTION

Materials and devices that dynamically change their shape, size, and electrical and mechanical properties in response to external stimuli have been studied for decades owing to their important applications as actuators, including artificial muscles, robotics, energy generators, sensors, and smart curtains (*1*–*3*). To date, substantial efforts have been devoted to develop smart actuators based on various active materials such as carbon-based materials (including carbon nanotube and graphene) (*4*, *5*), polymers (such as shape memory polymers, gels, conjugated polymers, and liquid crystal elastomers) (*6*–*9*), ceramic and alloy (*10*, *11*), etc. Multifarious environmental stimuli such as humidity (*12*), temperature (*13*), electricity (*14*), light (*15*), solvent (*16*), pH (*17*), or pneumatic stimulus (*18*) have been used to trigger alteration of the physical properties of these materials. Although some simple actuation behaviors have been realized via a single external stimulus by most of these actuators, there are still extreme challenges that are difficult to be tackled in practical use. For instance, it is difficult to further increase the deformation for carbon (carbon nanotube or graphene)–based actuators because their actuation is mostly caused by the difference in the thermal expansion of the bilayer structure (*19*). Most polymer- and gel-based actuators typically suffer from the relatively slow response speed, small-scale shape changes, and poor mechanical and thermal stability (*20*, *21*). The ceramic- and alloy-based actuators usually need high temperature or high voltage to be triggered (*22*, *23*). Most of these drawbacks could restrict their application potentials. Therefore, development of a smart soft actuator that can respond to diverse stimuli such as humidity, electricity, heat, or light, requiring low-power actuation, delivering fast actuation speed, large-shape deformation, programmable adaptability, and robust stability is highly desirable.

Exploration of previously unidentified combinatorial materials and rational design of device configuration are the key strategies to develop high-performance actuators. MXene ($Ti_3C_2T_x$), one of the new family of two-dimensional (2D) metal carbides (*24*) with excellent electrical conductivity (10^5 S/m) (*25*), thermal conductivity [55.8 W/(m K)] (*26*), and photothermal conversion capability (*27*) makes an interesting candidate for multiresponsive and potentially high-performance actuator. To the best of our knowledge, there is only one illustration of using MXene as an electromechanical actuator, as reported by Balke and coworkers (*28*). MXene ($Ti_3C_2T_x$) prepared as an electrochemical electrode experienced deformation strongly depending on the cation size, a maximal relative volumetric deformation of about 15% when the insertion of lithium-ion occurs (*28*). However, no cycling data were presented in the work, and the double-layer capacitance–based electromechanical actuator requires stringent sealing processes to secure the liquid electrolyte, which limits the field of applications. Our present work is aimed at using MXene as a multiresponsive soft actuator, exploiting the leaf-inspired sophisticated architecture with synergistic functional components and simple actuation mechanism.

RESULTS AND DISCUSSION

As a primary photosynthetic organ, a leaf is mainly composed of cuticle, epidermis, palisade mesophyll, vein skeleton, and stomata (Fig. 1, A and B) (*29*). Among them, the palisade mesophyll cell's function is to convert light energy into chemical energy such as carbohydrates. The vein skeleton makes the leaf robust and harder to degrade. There are some stomata in the outer covering layer of the leaf, which are beneficial to carbon dioxide, oxygen, and water vapor transport between the leaf and the atmosphere. All these elaborate structures and functional components synchronize cooperative function and make the leaf an effective photosynthetic vehicle (*30*). Moreover, these organized structures are generally responsible for the leaf swelling and shrinking upon water sorption and desorption. Inspired by the elaborate architecture and photosynthetic mechanism of a natural leaf, we designed an asymmetric bilayer-structured soft actuator with the single crystal 2D MXene ($Ti_3C_2T_x$) nanosheets mimicking the palisade mesophyll cell to harvest electric or light energy and convert it to thermal energy (Fig. 1C). Biocompatible cellulose nanofibers as the vein skeleton make the actuator more robust and enable rapid changes in shape. Polycarbonate (PC) filter membrane emulates the stomata and

[1]School of Materials Science and Engineering, Nanyang Technological University, 639798 Singapore, Singapore. [2]Department of Astronautic Science and Mechanics, Harbin Institute of Technology, Harbin 150001, P. R. China. [3]School of Chemical Engineering and Light Industry, Guangdong University of Technology, Guangzhou 510006, P. R. China.
*These authors contributed equally to this work.
†Corresponding author. Email: pslee@ntu.edu.sg

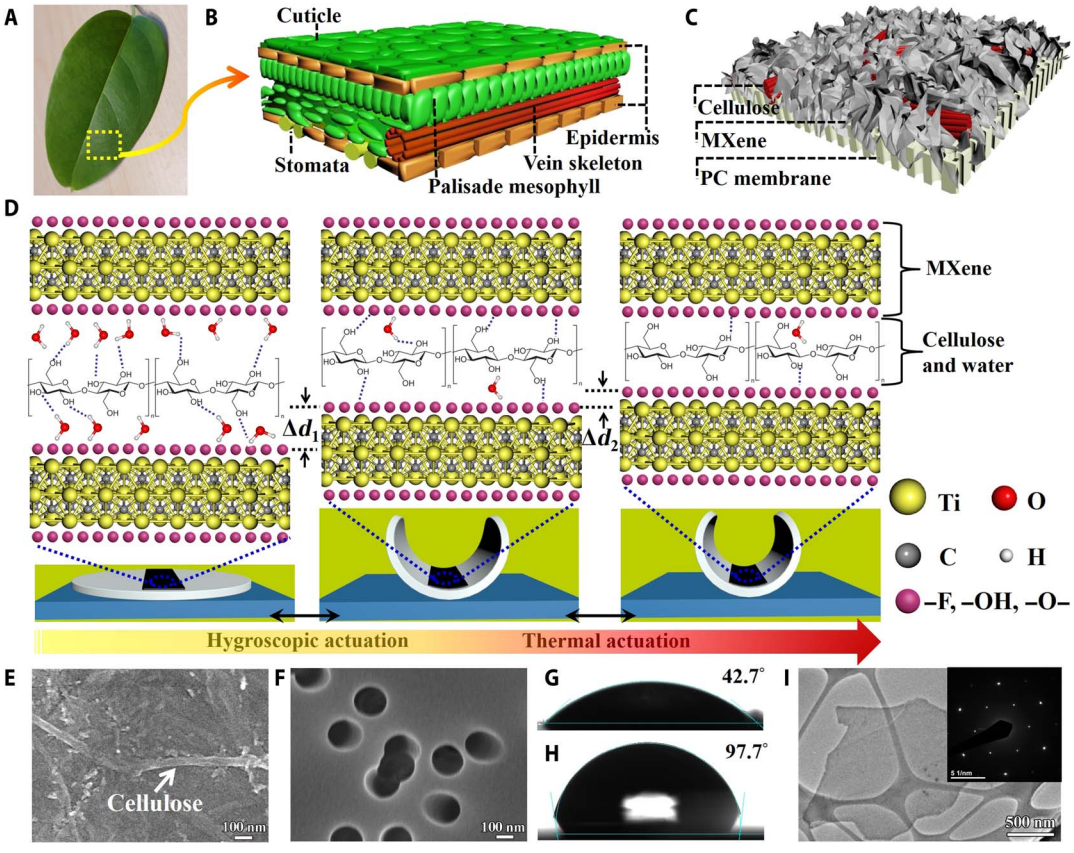

Fig. 1. The elaborate structure, components, and actuation mechanism of the MXene-cellulose–based actuator. (**A**) Photograph of a natural leaf. (**B**) Schematic diagram of a leaf structure. (**C**) Schematic diagram of the MXCC/PC bilayer-structured actuator, which is composed of MXCC and a PC filter membrane. (**D**) Actuation mechanism of the MXCC/PC bilayer-structured actuator. Macroscopic and microcosmic (involving H bonds) structure changes of the MXCC/PC bilayer-structured actuator in response to hygroscopic and thermal stimuli simultaneously (both hygroscopic and thermal actuation processes are controlled by electrical and NIR light actuation). Scanning electron microscopy images of the MXCC (**E**) and the PC filter membrane (**F**). Contact angle measurement of the MXCC (**G**) and PC filter membrane (**H**). (**I**) Transmission electron microscopy image of the 2D MXene nanosheet (inset: SAED pattern).

epidermis that facilitates water insertion/extraction into/from the MXene-cellulose composites (MXCC). We first integrated the cellulose nanofibers into the MXene nanosheets and then filtered them onto the porous PC membrane to create an asymmetric MXCC/PC structure. We prepared the MXCC ink by mixing MXene and cellulose nanofibrils. The hydrophilic functional groups (—OH and —O) on the surface of the MXene nanosheets and cellulose nanofibers endow the hygroscopic properties of the MXCC, analogous to the vein skeleton in the leaf (Fig. 1D, left). The dynamic hydrogen bonds between the adsorbed water, MXene, and cellulose can be associated and dissociated readily by small humidity fluctuations. Cellulose can increase the amount of adsorbed water in the composites, and the adsorbed water molecules, in turn, lead to enlarge d-spacings of 2D MXene nanosheets (more than 1.9 Å) and result in volume increase without changing the crystal structure of the MXene (fig. S1A). The increased absorbed water in MXCC was confirmed by Fourier transform infrared (FTIR) spectra (fig. S1B). Water gradually migrates from the cellulose into the MXene following a concentration gradient until an equilibrium state is achieved. Intermolecular hydrogen bonding between cellulose chain and MXene also serves as the binding agent that makes 2D MXene nanosheets tightly wrapped with the 1D cellulose nanofibers and form densely packed film on top of the PC membrane (Fig. 1E). The diameter of the cellulose nanofibers is less than 50 nm (fig. S2A). The PC membrane, being inert to water molecules (with hydrophobicity) and the uniform porous architecture (about 220 nm) throughout the whole membrane, accelerates the responsiveness by speeding up the water transportation (Fig. 1F). Because of the distinct hydrophilicity between the MXCC and PC membrane (Fig. 1, G and H), the unsymmetrical deformation can be instantly triggered by small humidity fluctuations in the ambient, which was accompanied by only a minute amount (44.4 μg cm^{-2}) of water sorption and desorption (Fig. 1D, right). Moreover, MXene nanosheets used in our work are nearly transparent to the electron beams (Fig. 1I). The average thickness of MXene nanosheets is about 1.32 nm (fig. S2, B and C), which is about two layers of $Ti_3C_2T_x$ stacked together (*31*). Selected area electron diffraction (SAED) patterns (inset of Fig. 1I) indicate that the MXene has a hexagonal structure and single crystallinity without obvious nanometer-scale defects.

We prepared a typical natural leaf–inspired adaptive smart soft actuator as detailed in Materials and Methods. The MXCC contains MXene:cellulose with an optimized weight ratio of 10:1 in deionized (DI) water under bath sonication for an hour. The process is simple and scalable, using filtration of the black MXCC ink on a PC membrane with the help of a mask to form a strip of MXene-cellulose ribbon (with dimensions of 40 mm by 10 mm by 5 μm) in the center of the PC membrane (fig. S3). The soft actuator maintained its flat, unwrinkled

form under ambient conditions with a relative humidity (RH) of about 70% (Fig. 2A, I and III). Notably, the MXCC/PC bilayer-structured soft actuator was found to autonomously bend toward the MXCC side at a lower RH of 10% (Fig. 2A, II and IV) and autonomously return to a flat state as the humidity increases. The soft actuator with the MXCC can bend to 88° and 62° in the downward and upward directions, respectively (the downward and upward directions in this work refer to the active MXCC facing down and up, respectively), in a reversible and repeatable manner. The bending angle is defined as the included angle of the PC membrane on opposite sides of the strip of MXene-cellulose ribbon (Fig. 2A, II and IV), which is captured by a video camera. The bending/unbending of the MXCC/PC bilayer-structured soft actuator was induced by the distinct water sorption/desorption capabilities of MXCC on a PC membrane. The hydrophilic MXene and cellulose endowed the water sorption/desorption; in contrast, the hydrophobic PC membrane is inert to humidity variation. Thus, the differences in hygroscopic properties lead to a mismatch in the volumetric changes between the MXCC and PC membrane during a variation of humidity. As a result, the contraction and expansion of the MXCC were created upon humidity reduction and increment. The variation of humidity accompanied by interfacial stress between the MXCC and PC membrane has led to the bending/unbending of the smart soft actuator systems.

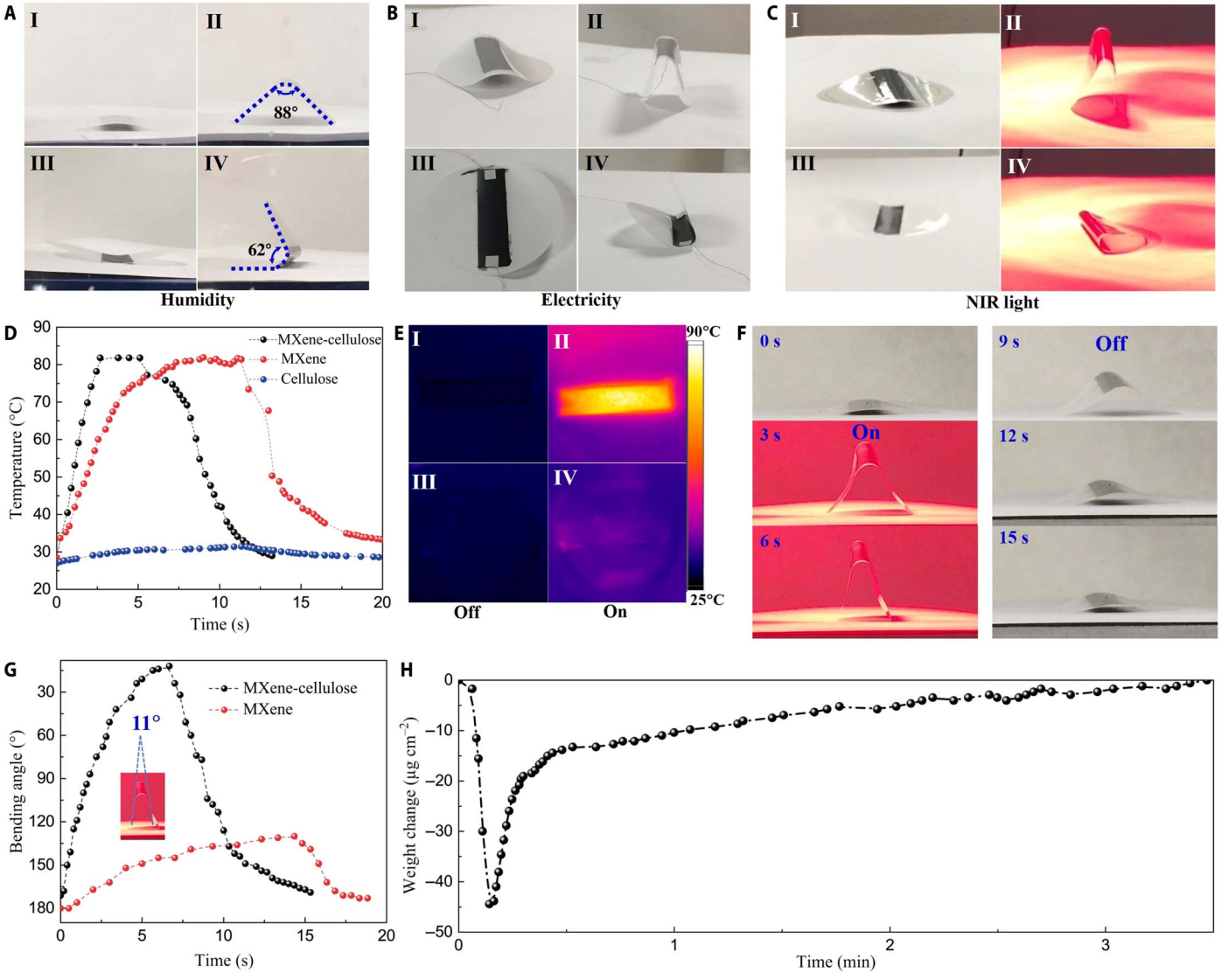

Fig. 2. Multiresponsiveness capabilities and performance of the soft actuators. (**A**) Humidity-responsive capability of the MXCC/PC bilayer-structured actuator [70% RH for AI and AIII, 10% RH for AII and AIV; the downward and upward directions refer to the active MXCC facing down (AI and AII) and up (AIII and AIV), respectively]. (**B**) Electricity-responsive capability of the MXCC/PC bilayer-structured actuator (power off for BI and BIII, and power on for BII and BIV). (**C**) NIR light–responsive capability of the MXCC/PC bilayer-structured actuator when NIR light was turned on and off with the active MXCC facing down (CI and CII) and up (CIII and CIV). (**D**) Temperature change profile as the NIR light was turned on (80 mW cm^{-2}) and off for MXCC-, MXene-, and cellulose-based actuators. (**E**) IR images of MXCC- and cellulose-based actuators without (EI and EIII) and with (EII and EIV) NIR light illumination (80 mW cm^{-2}). (**F**) Series of photographs showing the NIR light actuation process of the MXCC/PC bilayer-structured actuator. (**G**) Bending angle as a function of time during light turned on and off for the actuators based on MXCC and MXene, respectively. (**H**) Corresponding weight change as a function of time during light turned on and off for the MXCC/PC bilayer-structured actuator. (Photo credit: Guofa Cai, Nanyang Technological University.)

To quantitatively analyze the actuation performance driven by humidity variation, we fabricated an actuator strip (35 mm by 10 mm by 25 μm) with the square MXCC (10 mm by 10 mm by 5 μm) in the center. The bending degrees of the actuator strip under different RHs were evaluated (fig. S4). The excellent actuation performance and controllable bending angles in various humidity levels were illustrated by decreasing the RH from 90 to 5% systematically. The bending angles of the actuator show the corresponding decrease from 210° to 45°. In addition, the bending angles linearly reduce with decreasing RH in the range of 50 to 5%. The angle change (165°) is much larger than that of the humidity-responsive poly(ethylene glycol) diacrylate hydrogel–based actuator (with an angle change of about 20°) (*32*).

Considering its excellent electrical conductivity and thermal conductivity, MXene can serve as a heater to rapidly convert electrical or light energy into thermal energy. Nevertheless, the PC membrane is inert to both electrical and light stimuli. The rapid water desorption at high temperature can cause the marked contraction of the MXCC layer. The MXCC layer becomes flat when the temperature recovers to room temperature at 25°C. In contrast, the PC membrane is expanded when heated and contracted when temperature is lowered (thermal expansion coefficient of the PC membrane is about 6.5×10^{-5}/K) (*3*). The thermally induced bending curvature of our MXCC/PC bilayer-structured soft actuator can be expressed as (*33*)

$$\varepsilon \propto (\alpha_{PC} - \alpha_{composites})\Delta T + \beta_{composites}\Delta C_{composites} - \beta_{PC}\Delta C_{PC} \quad (1)$$

where ε denotes the bending curvature of the MXCC/PC bilayer-structured soft actuator, and α_{PC} and $\alpha_{composites}$ refer to the respective thermal expansion coefficient for the MXCC and PC membrane. ΔT is the temperature variation, β_{PC} and $\beta_{composites}$ are the respective hygroscopic expansion coefficient for the MXCC and PC membrane, and ΔC_{PC} and $\Delta C_{composites}$ are the variation of moisture concentration in the PC membrane and MXCC, respectively, due to the temperature gradient. On the basis of the above analysis, MXCC has a smaller thermal expansion coefficient and a larger hygroscopic expansion coefficient compared to the PC membrane. Therefore, it can maximize the actuation performance of the MXCC/PC bilayer-structured soft actuator by combining both thermal expansion and hygroscopic expansion. Furthermore, it holds great promise for the MXCC/PC bilayer-structured soft actuator in multiresponsive applications. We investigated the electrical actuation of our device in a standard electrothermal actuator configuration in which both ends of the MXene-cellulose strip were connected to two superfine copper wires (Fig. 2B). In agreement with the earlier hygroscopic actuation experiment, the actuator had a relatively flattened state before electrical actuation (Fig. 2B, I and III), but the actuator can be uplifted (the central MXCC area was lifted from the substrate and higher than the edges of the PC membrane) or fold itself (the central MXCC area remained in contact with the substrate, but parts of the PC membrane edges were lifted from the substrate and the opposite PC edges were infinitely near with each other) from a flat status after applying a small voltage on the MXCC facing downward or upward, respectively (Fig. 2B, II and IV). We found that the bending angle almost linearly decreases with increasing electrical power, and the maximum change in bending angle of 147° (from 180° to 33°) can be achieved with a power of 0.106 W cm^{-2} (operating at 5.1 V; fig. S5A). Moreover, our MXCC/PC bilayer-structured soft actuator only needs a low voltage of 5.1 V to achieve the extreme actuating motions (fig. S5B). Compared to humidity actuation, the larger bending angle changes are achieved by electrothermal actuation, confirming the synergistic effect of thermal expansion and hygroscopic expansion. The figure of merit of our actuator exceeds those carbon-based bilayer actuators, which usually need more than 10 V as driving voltage (*4*, *34*).

Because of the excellent optical absorption and photothermal conversion abilities of MXene and the superb electrothermal actuation performance of the MXCC/PC bilayer-structured soft actuator, we anticipate that our smart soft actuator has tremendous potential in photoresponsive actuator applications. Moreover, among a variety of the above-mentioned external stimuli, light stimulus is especially attractive owing to its wireless characteristics and spatial and rapid temporal controllability. We studied the effect of the near-infrared (NIR) light actuation on the properties of the soft actuator detailed as follows. When placing the flat MXCC/PC bilayer-structured soft actuator with the MXCC facing downward or upward, it can instantly stand up or fold itself, respectively, upon NIR light irradiation (illumination intensity of 80 mW cm^{-2}) (Fig. 2C and movie S1). We recorded the temperature variation and bending angles of the soft actuators during NIR light irradiation. NIR light irradiation can locally heat the bilayer-structured actuator within the MXene area. Once NIR light was turned on and off, the instant temperature rise and decline were observed from the MXCC/PC and MXene/PC bilayer-structured soft actuators; nevertheless, no obvious temperature change was found in the cellulose/PC bilayer-structured actuator (Fig. 2D). Of interest, the ramp rate (which is defined as the time required for the actuator to reach 90% of its maximum temperature variation) of the MXCC/PC actuator is 2.3 s, which is faster than that of the MXene/PC actuator (5.3 s). The rapid speed of the MXCC/PC actuator is attributed to the junctions between the MXene nanosheets that are tightly bridged by the 1D cellulose nanofibers due to the numerous hydrogen bonds among them. The sheet resistance of the MXene film after mixing 10% of cellulose nanofibers is reduced from 12.6 to 10.3 ohm sq^{-1}, which further confirmed the enhanced binding of the composite film. Although the individual components of MXene or cellulose materials have poor actuation performance, their composites achieve remarkable synergistic actuation motions. The temperature of both the MXCC/PC and MXene/PC bilayer-structured soft actuators can rapidly reach to about 80°C (with a temperature change of about 54°C) within several seconds (Fig. 2E, movie S2, and fig. S6). The temperature change and ramp rate achieved by our actuator are larger and faster than those of the recently reported thermal-responsive graphene oxide (GO)/poly(*N*-isopropylacrylamide) bilayer actuator, which presented a temperature change of about 23°C under NIR irradiation for 90 s (the temperature does not reach a plateau within this time range) (*35*). The temperature changes during the NIR irradiation are accompanied by the shape changes of the actuator (Fig. 2F). The time scale of the bending angle curve of the MXCC/PC actuator is consistent with the temperature variation curve under the same conditions, which confirms the hypothetical photothermal actuation mechanism and instant responsive characteristic. Under NIR irradiation with illumination intensity of 80 mW cm^{-2} for 6.5 s, the flat MXCC/PC actuator can bend to 11° with an angle change of about 169° (Fig. 2G). In contrast, the MXene/PC actuator presents slower actuation speed and smaller-scale shape changes due to the lack of the skeletal cellulose nanofibers. The performance of our MXCC/PC actuator outperforms the state-of-the-art GO-polydopamine composites/reduced GO and thermal-activated single-wall carbon nanotube/PC–based bilayer actuators, which can bend from their flat status to 60° (angle change is 120°) and 90° (angle

change is 90°), respectively, under a higher illumination intensity of 100 mW cm^{-2} (*3*, *36*). The angle change achieved by our MXCC/PC actuator is also superior to that of the recently reported GO–carbon nanotube composite/polydimethylsiloxane (PDMS) bilayer actuators with the maximum angle change of 90° achieved by a high illumination intensity exposure of 500 mW cm^{-2} (*37*). We further monitored the weight changes of the MXCC/PC actuator during NIR light irradiation for 5 s at a constant humidity of 70% RH. We found that only 0.77 mg of water was released from the MXCC/PC actuator; this corresponds to a weight loss of 44.4 μg cm^{-2}, which is only 1.72 weight % (wt %) of its initial weight (Fig. 2H). The weight changes of our MXCC/PC actuator during the actuation process were much lower than that of the pentaerythritol ethoxylate (PEE)–polypyrrole (PPy)–based actuator, which required an adsorption of 10 wt % of water (*1*). Therefore, our MXCC/PC actuator can be triggered by low power and exhibits rapid response. Moreover, the weight of the MXCC/PC actuator can fully recover to its initial weight after leaving the actuator in ambient air for about 3 min. For comparison, we fabricated an MXCC/PDMS bilayer structure by transferring MXCC on a compact PDMS substrate of similar thickness as the PC membrane. It can be seen that the weight change speed of the MXCC/PDMS bilayer structure is slow, and it could not be fully recovered when the NIR light is turned off for more than 5 min (fig. S7), indicating that the porous PC membrane facilitates water insertion/extraction into/from the actuator. The PC membrane has a large water permeability coefficient of 1780 ± 30 Barrer (*38*), which is consistent with its facile water transport property.

We further evaluated the photoinduced mechanical force under NIR light irradiation on a mechanical analyzer. An actuator strip (35 mm by 10 mm by 25 μm) with the square MXCC (10 mm by 10 mm by 5 μm) in the center was clamped and preloaded with a prestrain of 0.15% to keep the film straight and tight (fig. S8A); the mechanical force generated in the actuator can be measured. Upon NIR light irradiation (50 mW cm^{-2}), the static force generated by the mechanical analyzer to maintain the actuator at the constant strain slightly reduces first and then markedly increases accompanied by a minute expansion of the actuator at the beginning and a large constriction after (Fig. 3A). We propose the following as an underlying mechanism for the unique characteristic of our MXCC/PC actuator. Instant heat will be generated once the NIR light is turned on, which would lead to a slight expansive force (1.7 mN) and expansion (0.0006%) in the actuator (cyan dashed circle indicated in Fig. 3A); hence, the mechanical analyzer reduces an equal force at the same time to counteract the expansive force of the actuator and maintain the actuator at a constant strain (0.15%). Thereafter, a large contractile force (43.4 mN) and shrinkage (0.088%) are generated in the actuator due to the adsorbed water being quickly evaporated from the MXCC at the high temperature (Fig. 3A). Accordingly, the mechanical analyzer increases equal force to balance the contractile force and stretches the actuator to the constant strain. Once the NIR light is turned off, the contractile force generated by the actuator fades off. As a result, the excessive counteracting force generated by the mechanical analyzer will stretch the actuator over the

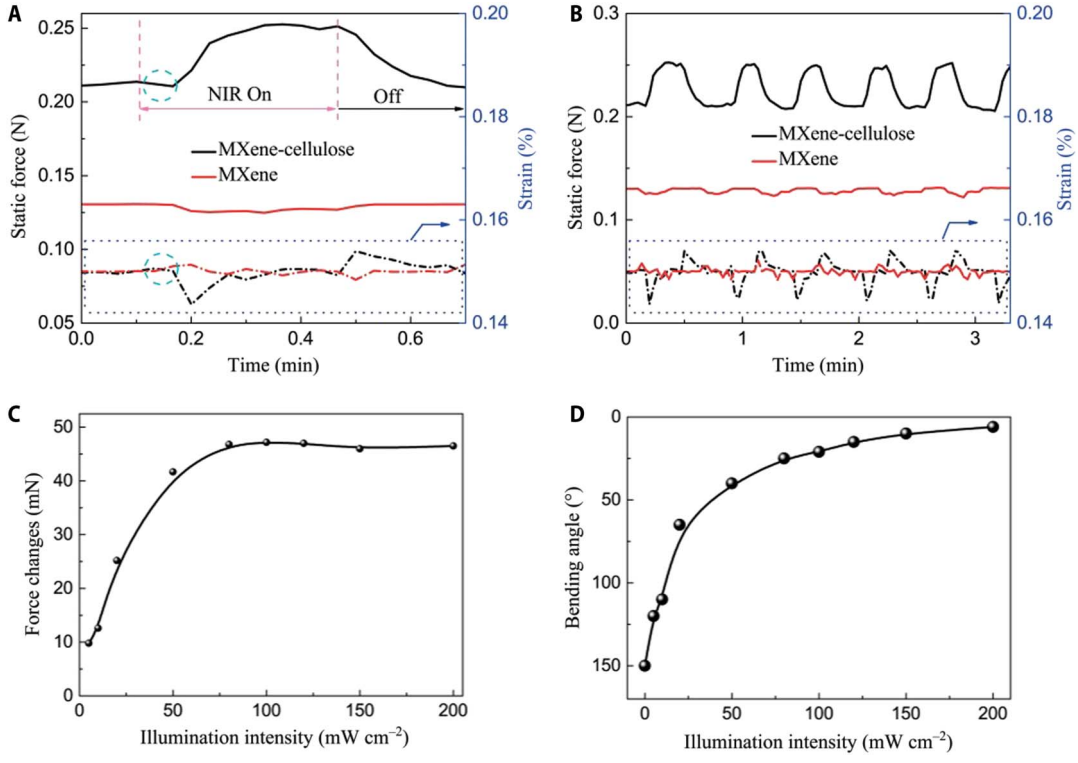

Fig. 3. Mechanical performance and motions of the MXCC/PC bilayer-structured actuator caused by NIR light. (**A**) Typical static force and strain changes of the MXCC- and cellulose-based actuators during one actuation cycle when NIR light illumination was turned on and off (50 mW cm^{-2}). (**B**) Plot of the static force and strain of the MXCC- and cellulose-based actuators as a function of time for five consecutive NIR light on and off cycles, indicating the reversible, stable, and rapid actuation process. (**C**) Static force changes of the MXCC-based actuator under different NIR illumination intensities (from 5 to 200 mW cm^{-2}). (**D**) Bending angle of the MXCC-based actuator under different NIR illumination intensities (from 5 to 200 mW cm^{-2}).

constant strain by 0.004%. After that, the excessive force and the strain of the actuator will recover to their initial states as water saturation is achieved in the actuator. In a controlled MXene/PC actuator without cellulose nanofiber, we observed only negligible expansive force and residual strain around 0.15%. The actuation process of the MXCC/PC actuator is rapid and reversible (Fig. 3B), and no obvious degradation in strain and static force changes after 50 cycles (fig. S8, B and C). We also evaluated the stability by repeatedly applying NIR light to the actuator, and we measured the weight at each 50 cycles after turning off the NIR light for about 5 min (fig. S8D). The weight of the actuator was kept constant by alternately switching the NIR light on and off for 1000 cycles, indicating a robust reversibility of the actuator. We investigated the static force change and bending angle as functions of NIR light intensity for the same actuator after irradiation for 5 s. The static force and bending angle changes increased markedly with increasing NIR light intensity from 0 to 80 mW cm^{-2} (Fig. 3, C and D). After that, the static force changes reached almost a constant value of about 45 mN, and the change in bending angle slowly increased. The force generated by the MXCC/PC actuator is much larger than that of the reduced graphene oxide (RGO)/GO and poly(ionic liquid) and poly(3-cyanomethyl-1-vinylimidazolium bis(trifluoromethanesulfonyl)imide)/carboxylic acid–substituted pillar[5]arenai-based actuators (*5*, *39*). The maximum force achieved by these actuators was only 1.6 and 0.75 mN, respectively. These results illustrate that parts of the adsorbed water in the actuator can be evaporated within illumination intensity of 80 mW cm^{-2}, and most of the adsorbed water in the actuator can be quickly evaporated when the illumination intensity exceeds 80 mW cm^{-2}. The flat actuator strip can bend to 6° with illumination intensity of 200 mW cm^{-2}. The stress generated from the MXCC-based actuator at illumination intensity of 100 mW cm^{-2} is 0.18 MPa [the stress is calculated by $\sigma = F/A$, where F is the force (45 mN) generated by the MXCC-based actuator at illumination intensity of 100 mW cm^{-2}, and A is the cross section of the MXCC-based actuator (25 μm by 10 mm = 2.5×10^{-7} m^2)], which is comparable to the mammalian skeletal muscle (~0.35 MPa) and previously reported soft actuators (~0.1 MPa) (*40*,*41*).

We studied the structure change of the MXCC/PC and MXene/PC actuators under different illumination intensities using in situ x-ray diffraction (XRD) measurements (Fig. 4A). Only the diffraction peaks of MXene ($Ti_3C_2T_x$) were observed in the XRD patterns of the MXCC/PC and MXene/PC actuators, indicating an amorphous characteristic of cellulose and PC membrane. The (002) diffraction peak of MXene is downshifted to 1.9 Å after mixing with cellulose (fig. S1A). In addition, the wider width and weaker intensity in the MXCC/PC actuator illustrate the increased randomness of the interlayer spacing of layered MXene with cellulose. The —OH group of cellulose can interact with the hydrophilic functional groups of MXene through hydrogen bonds. Furthermore, cellulose can enhance the hygroscopy of MXene. Meanwhile, cellulose and MXene are bridged by water molecules through intermolecular hydrogen-bonding interaction, which enlarged the d-spacing of stacked MXene nanosheets. Under NIR illumination at intensities of 50, 100, and 150 mW cm^{-2}, the (002) diffraction peak of the MXCC/PC actuator moved to 6.70°, 6.81°, and 6.95°, respectively, verifying the decreased interlayer d-spacing. Notably, the corresponding interlayer d-spacing of the MXCC/PC actuator was decreased from 14.8 Å to 13.2, 12.98, and 12.7 Å accompanying large shrinkages of 1.6, 1.82, and 2.1 Å under illumination intensities of 50, 100, and

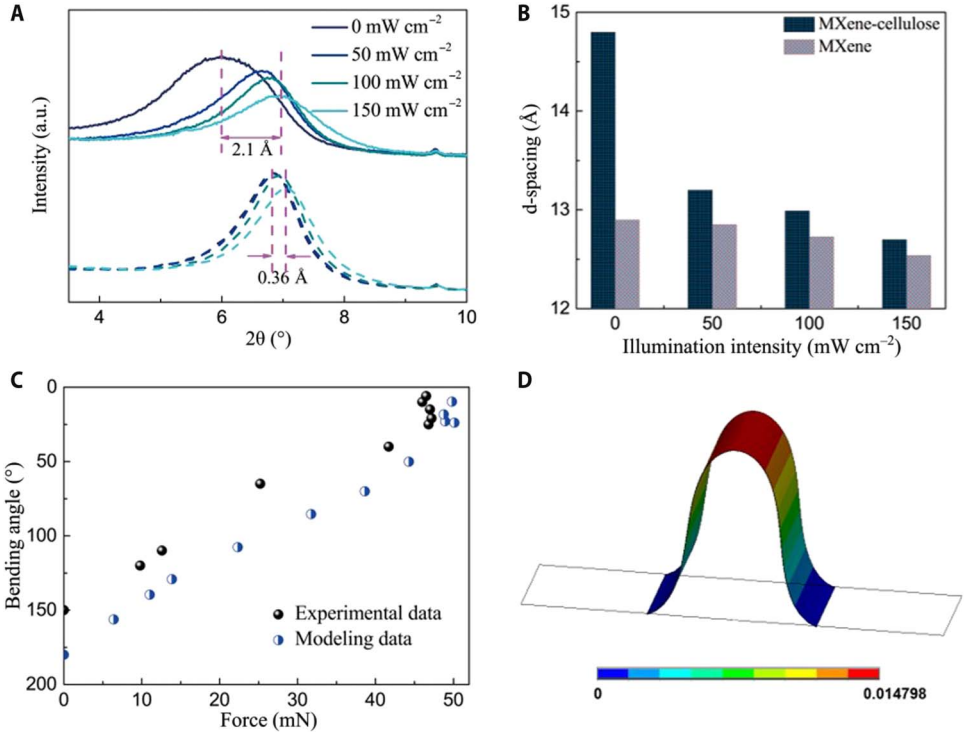

Fig. 4. Structure change under different NIR illumination intensities and mechanical modeling. (**A**) XRD patterns of MXCC- and MXene-based actuators under different NIR light illumination intensities (solid lines, MXCC-based actuator; dashed lines, MXene-based actuator). (**B**) Corresponding d-spacing of the MXCC- and MXene-based actuators under different NIR light illumination intensities. (**C**) Simulated and experimental results of the MXCC-based actuator. (**D**) Simulated results of the MXCC-based actuator under NIR light illumination.

150 mW cm^{-2}, respectively (Fig. 4B). Nevertheless, the MXene/PC actuator only presents slight diffraction peak shift and d-spacing changes at the same illumination intensities. Only small shrinkages of 0.05, 0.17, and 0.36 Å were observed for the MXene/PC actuator under illumination intensities of 50, 100, and 150 mW cm^{-2}, respectively. These results further confirmed the mechanism and the excellent performance of our MXCC/PC actuator under NIR light irradiation conditions.

We investigated the mechanical behavior by a finite element (FE) model to further understand the actuation process of the MXCC/PC actuator. On the basis of the above results, the actuation is mainly attributed to mismatch in the volume changes between the MXCC and PC membrane caused by the contractile and expansive force upon NIR irradiation. Therefore, we can control the actuating motions of the actuator by adjusting the relatively contractile and expansive force. We considered the model with thermal mechanical coupling capabilities, and mesh was generated according to the specifics of the design (fig. S9). We also implemented displacement and symmetrical constrains for the boundary conditions in the FE model. We calculated the effect of force generated under different illumination intensities (from 5 to 200 mW cm^{-2}) on the bending angle. As a result, the modeling results matched our experiments very well (Fig. 4C). Both results indicate that the bending angle decreases with increasing contractile force, which was generated by desorbed water until a constant value. After that, the contractile force does not change a lot, but the bending angle slowly decreased because of the increased contractile force (almost equal to the thermal expansive force) by further increasing the illumination intensity. From the modeling, the actuator can also reversibly bend from a flat state to a small angle (Fig. 4D and movie S3).

We demonstrated the programmable actuation behavior of the soft actuator by using the MXCC as active hinges. The active hinge refers to a narrow, rectangular region, which localized a bend within this region and results in the opposite plates on each side bending at an angle with respect to each other. A series of sophisticated configurations were constructed by a rational design of the hinge's number and size on the PC membrane (Fig. 5). First, to keep the sum area of MXCC equivalent to the previous actuator in Fig. 2, we fabricated two hinges of the same size (40 mm by 5 mm by 5 μm) and symmetrically positioned them on the PC membrane with a gap of 5 mm (Fig. 5A). With the MXCC facing upward, the flat actuator can quickly and reversibly change its appearance to a "U" shape upon NIR light irradiation and recover to a flat state when the NIR light is turned off. In addition, we observed an inverted U-shape change when placing the actuator with the MXCC facing downward. Note that the U-shape curvature can be deepened by increasing the gap between the two active hinges when MXCC is facing upward (fig. S10A). However, the shape change will be smaller with the MXCC facing downward. The actuator could not be uplifted when the gap between the two active hinges is 10 mm with the MXCC facing downward, because the force generated by two active hinges is too weak to lift the wide PC membrane between the two active hinges. When hinge number was increased to 3 and symmetrically distributed on the PC membrane with a gap of 7 mm (Fig. 5B), the flat actuator can quickly and reversibly change its appearance between flat and a "trefoil arch" shape upon turning the NIR light on and off, irregardless of the MXCC facing upward or downward. Furthermore, more complex geometries such as self-folding box and self-blooming flower could also be realized with this simple and convenient adaptable construction. When some fine hinges were uniformly distributed on the cross-shaped PC membrane, it can fold by itself into a box under NIR light. Then, the box unfolded back into its original state after the NIR light was turned off (Fig. 5C and movie S4). A biomimetic flower was further constructed by using the PC membrane with uniformly distributed MXene-cellulose hinges as the petals (Fig. 5D). The petals open and the flower blooms before NIR light irradiation. Once exposed to the NIR light, the petals close rapidly (movie S5). The reversible actuation illustrated that our MXCC/PC actuator is programmable and controllable. We further calculated the energy density and power density of the MXCC-based actuator, which are 0.737 and 0.92 W kg^{-1}, respectively (fig. S10B). The power density of the MXCC-based actuator is comparable to the PEE-PPy actuator (0.9 W kg^{-1}) (*1*).

We explored various smart devices based on the MXCC/PC soft actuator, such as a worm-like robot, smart switch, an information encryption device, and IR dynamic display and camouflage (Fig. 6). Because the output force (f) and the bending angle (θ) of the MXCC/PC bilayer actuator are dependent on the width of the MXCC, the relationship can be described as follows (*36*)

$$f = kl \tag{2}$$

and

$$\theta = 180\text{-}\frac{1080kl^2(d_1 + d_2)}{\pi(E_1\, d_1^3 + E_2\, d_2^3)} \tag{3}$$

where k and l refer to the scale factor and width of the MXCC strip, respectively. E_1 and E_2 and d_1 and d_2 are Young's moduli and thickness of the MXCC and PC membrane, respectively. Equations 2 and 3 illustrate that the output force and bending angle of the actuator can be controlled through adjusting the width of the MXene-cellulose strip. Therefore, an NIR light–driven worm-like robot can be fabricated by filtering three MXene-cellulose strips with different widths on the rectangular PC membrane (Fig. 6A). Upon NIR irradiation, the whole actuator bent upward into a trefoil arch because of the contracted MXene-cellulose strip (Fig. 6B). Meanwhile, the end of the actuator

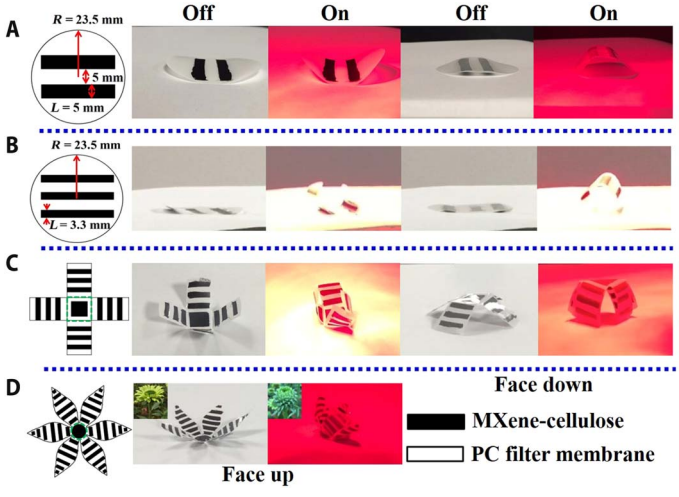

Fig. 5. Representative programmable motions for the MXCC/PC bilayer-structured actuator. (**A**) Double folding U-shape actuator. (**B**) Trefoil arch–shaped actuator. (**C**) Self-folding box. (**D**) Self-blooming flower. Green dashed lines in (C) and (D) (left diagram drawing) are the slight creases created on the bottom of the box and flower to make the self-folding box and self-blooming flower work well under NIR irradiation. (Photo credit: Guofa Cai, Nanyang Technological University.)

near the narrow MXene-cellulose strip will move forward because of the smaller force produced by the narrow strip, and the other end was anchored on-site. When the NIR light was turned off, the MXene-cellulose strips adsorbed water from the environment and became swollen, which caused the end of the actuator near the wider MXene-cellulose strip to move forward, and the other end was anchored on-site because the push force produced by the wider strip is larger than the friction force that existed between the actuator and the substrate (movie S6). In this way, the actuator unidirectionally walked in a step-by-step manner by alternately switching the NIR light on and off. It is unexpected that the actuator can move about 5 mm with one walking cycle (Fig. 6C and movie S6). We also presented a smart switch by the MXCC/PC soft actuator, which can be controlled by wireless NIR light. The smart switch was constructed by patterning cross-shaped MXCC on the PC membrane; the width of one MXene-cellulose strip is 10 mm, and the other is 5 mm (Fig. 6D). The NIR responsiveness property of our switch was also demonstrated on a complete circuit composed of a smart watch with the MXCC/PC soft actuator as the conductor (Fig. 6E). The smart watch could not operate without NIR light irradiation (Fig. 6F). Upon NIR light irradiation, the actuator will bend versus the wider MXene-cellulose strip, and the narrow strip can be the conductor processing circuit; the smart watch can be successfully powered at the same time (Fig. 6G). The circuit became an open electrical circuit, and the smart watch was switched off when the NIR light was turned off (movie S7).

We lastly illustrate the multifunctionality of our soft actuator in information encryption, IR dynamic display, camouflage, temperature regulation, etc. Information encryption technologies, such as widespread barcode, QR code that are machine-readable optical label, have been developed for many years. These encrypted codes are not really safe, especially to the infocom sector. Here, we illustrate that our MXCC/PC soft actuator can be a novel information encryption device, and the preparation procedure is scalable and low cost because the versatile MXCC ink can be coated not only on the PC membrane but also on an ordinary flexible A4 paper (Fig. 6H). Considering the programmable feature of the MXene-cellulose ink, we can fabricate any desired pattern, so as to convey the information via local heating of the pattern through NIR light or electricity. This information is only IR camera readable and is invisible to the human naked eye. In this way, information encryption and display can be achieved successfully (Fig. 6I). We evaluated the encryption and display abilities of our MXCC/PC systems (Fig. 6J). The numbers from 0 to 9 and a letter "H" can be displayed under an IR camera by locally irradiating part of the pattern via NIR light. An apparent temperature difference between the active area and the surrounding membrane of about 5.5°C can be revealed via an IR camera. However, it looks the same to the naked eye whether with or without NIR irradiation. In addition, integrating different functionality into one system to achieve camouflage, display, and actuation is important and useful. We presented these functions by patterning MXCC into a butterfly

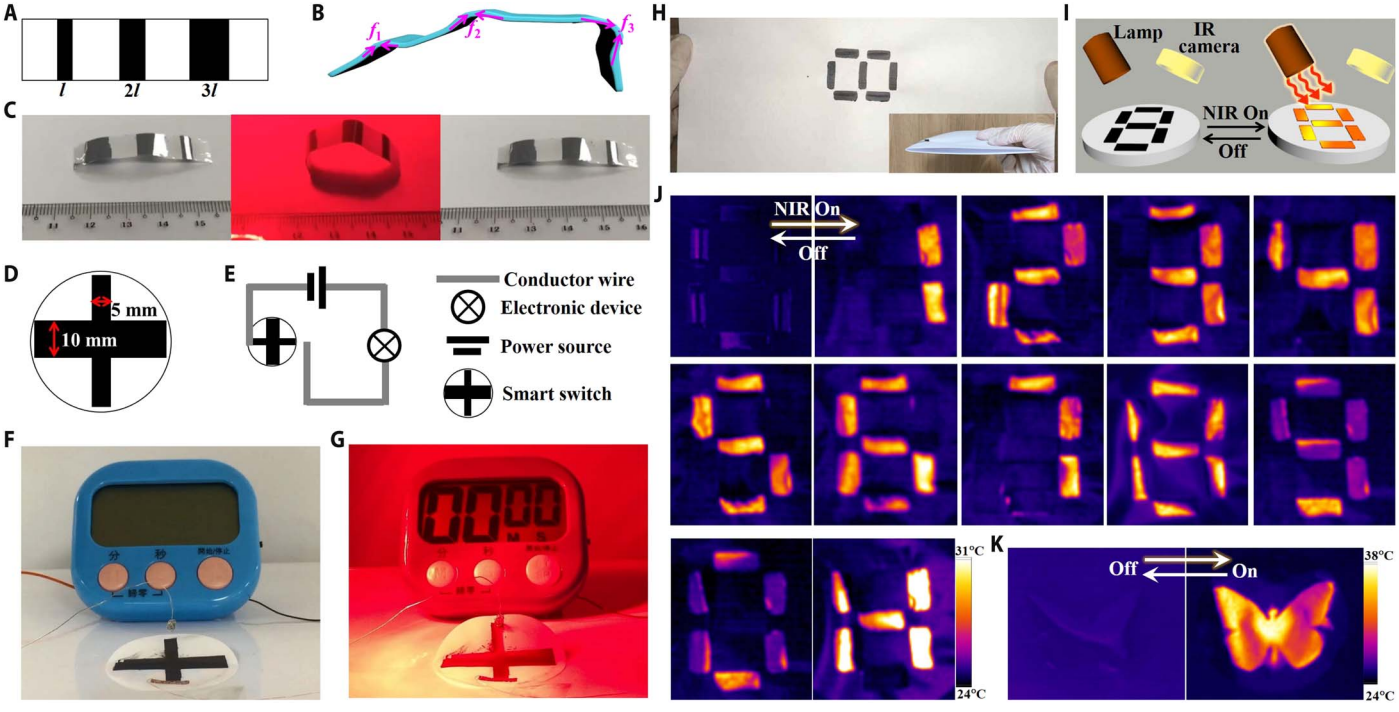

Fig. 6. Multifunctional smart devices based on MXCC actuators. (**A**) Configuration of a worm-like robot. (**B**) Mechanical model of the worm-like robot under NIR light irradiation. (**C**) Photographs of the worm-like robot crawling progressively driven by NIR light irradiation. (**D**) Configuration of a smart light–controlled switch. (**E**) Schematic diagram of a light-controlled circuit diagram. The circuit comprises light-controlled switch in series with a smart watch (**F**) with and (**G**) without NIR light illumination (80 mW cm^{-2}). (**H**) Photographs of the patterned MXCC on ordinary A4 paper, illustrating the versatile and programmable MXene-cellulose ink, scalable and low-cost fabrication, and flexible and foldable device (inset). (**I**) Schematics of the device with patterned MXCC before and after NIR light illumination. (**J**) IR camera images of the patterned device before and after local NIR irradiation to demonstrate information encryption and display applications. (**K**) IR camera images of a patterned device with a butterfly-silhouetted MXCC device before and after local NIR irradiation to illustrate the camouflage, display, and actuation applications. The patterned device changes its thermal appearance and stands out from the background upon NIR irradiation. (Photo credit: Guofa Cai, Nanyang Technological University.)

silhouette on the PC membrane and then imaging it with a thermal IR camera under an NIR irradiation above the device. Our device can successfully conceal itself under IR visualization even without NIR irradiation, because only a minute temperature difference with the surroundings was detected, which effectively made it invisible to the IR camera in the ambient temperature of ~25°C (Fig. 6K). However, a lifelike butterfly and an apparent temperature difference of about 14°C with the surroundings were displayed upon NIR irradiation. Moreover, the appearance changes were rapid, real, and reversible under IR visualization (movie S8). These devices confirm that our MXCC/PC membrane can serve multiple functions in smart soft systems such as actuation, information encryption, display, camouflage, and temperature regulation. We believe that new materials, rational design, low-cost fabrication, simple operation, and synthetic strategies of our MXCC/PC membrane systems would make them accessible and potentially useful to broad scientific and engineering fields.

CONCLUSIONS

In conclusion, we have developed and established a new class of multiresponsive materials and devices with an unprecedented integration of properties inspired by the structure and function of the natural leaf. First, our MXCC/PC membrane systems mimics several crucial features of a natural leaf from its microstructure to its photosynthesis capability (energy-harvesting and conversion capacities). Second, our MXCC/PC membrane bilayer actuators feature strong figures of merit and capabilities that outperform, or are on par with, state-of-the-art multiresponsive actuators. Third, our devices have been inherently designed for programmable actuation, adaptive integration, and low-cost manufacturability. Last, the devices may enable potentially promising applications in soft robots, smart switch, information encryption, IR dynamic display, camouflage, thermal regulation, etc. Ultimately, these explored materials and systems present novel possibilities for numerous revolutionized technologies and to benefit a number of aspects of our daily life.

MATERIALS AND METHODS

Synthesis of MXene ($Ti_3C_2T_x$) nanosheets

MXene ($Ti_3C_2T_x$) nanosheets were synthesized and delaminated according to the modified LiF/HCl method (*42*). The etching solution was prepared by dissolving 3.2 g of lithium fluoride (LiF) into 30 ml of 9 M hydrochloric acid (HCl). Then, 2 g of Ti_3AlC_2 powder (≥98%; Famouschem Technology Co. Ltd.) was slowly added into the etching solution over the course of 5 min with agitation of a magnetic stir bar. The etching process continued for 12 hours under magnetic stirring at room temperature. Thereafter, the reaction products were washed with DI water and centrifuged for several cycles under 10,000 rpm until reaching a pH value between 5 and 6. The sediment was then subjected to sonication with Ar gas bubbling for 1 hour, after which dispersion was carried out in the centrifuge at 3000 rpm for 30 min to eliminate the unexfoliated $Ti_3C_2T_x$ MXene sheets. Last, the MXene nanosheet solution was obtained and stored at 4°C until use.

Synthesis of Mxene-cellulose composite ink

The MXCC ink was prepared by mixing MXene and cellulose nanofibrils in DI water under bath sonication for an hour. The optimized weight ratio of MXene and cellulose was 10:1 in the ink. Beyond this weight ratio, the conductivity and the actuation performance will be degraded. The concentration of MXCC was 0.5 wt %.

Fabrication of the MXCC/PC bilayer-structured actuator

The MXCC/PC bilayer-structured actuator was fabricated by filtering the MXCC ink on a PC filter membrane (Millipore GTTP) with a pore size of about 220 nm. The patterned actuator was fabricated with the help of a mask during the filtering process. The MXene/PC and cellulose/PC bilayer-structured actuators were also prepared on the PC filter membrane with the same parameters for comparison purposes. The actuators were rinsed with DI water after filtration. Last, the actuators were left in air at ambient temperature for 2 hours to dry. Solution filtering of the MXCC ink was also performed on an A4 size paper as a membrane.

Characterization

XRD [Bruker D8 Advance with Cu-Kα radiation (λ = 1.541874 Å], scanning electron microscopy (JEOL 7600F), a Spectrum GX FTIR spectrometer (PerkinElmer Inc.), transmission electron microscopy (JEOL 2010), and an atomic force microscope (Asylum Research) were used to characterize the structure, morphology, and composition of Mxene, cellulose, and their composites. The static force and strain generated by the actuators upon NIR light irradiation were measured on a universal a mechanical analyzer (DMA Q800). The wavelength range of the NIR lamp used in this study was from 650 to 1050 nm. For experiments on information encryption and display demonstration, local heating was performed by exposing selective MXCC shapes to NIR light; the other MXCC area was covered by a mask.

Mechanical modeling

Mechanical modeling was carried out on an ANSYS 19.0 by an FE model based on the constitutive equation. In this case, the 3D problem of the stress-strain relations can be calculated as follows

$$\{\varepsilon\} = [C]\{\sigma\} \tag{4}$$

or $\{\sigma\} = [E]\{\varepsilon\}$ and $[C] = [E]^{-1}$.

The equation above is known as the generalized Hooke's law. The matrix C is called the material compliance matrix, while its inverse E is known as the material stiffness matrix or, more commonly, the constitutive matrix.

The compliance matrix for an isotropic elastic material can be described as

$$\begin{aligned}
\varepsilon_{11} &= \frac{1}{E}[\sigma_{11} - \nu(\sigma_{22} + \sigma_{33})] \\
\varepsilon_{22} &= \frac{1}{E}[\sigma_{22} - \nu(\sigma_{11} + \sigma_{33})] \\
\varepsilon_{33} &= \frac{1}{E}[\sigma_{33} - \nu(\sigma_{11} + \sigma_{22})] \\
2\varepsilon_{23} &= \frac{\sigma_{23}}{G}, 2\varepsilon_{13} = \frac{\sigma_{13}}{G}, 2\varepsilon_{12} = \frac{\sigma_{12}}{G}
\end{aligned} \tag{5}$$

E is the Young's modulus, ν is the Poisson's ratio, and G is the shear modulus. They are referred to as the engineering constants. The shear modulus G is related to the Young's modulus E and Poisson's ratio ν by the expression $G = \frac{E}{2(1+\nu)}$.

The equations above can be written in the following matrix form

$$\begin{bmatrix} \varepsilon_{11} \\ \varepsilon_{22} \\ \varepsilon_{33} \\ 2\varepsilon_{23} \\ 2\varepsilon_{13} \\ 2\varepsilon_{12} \end{bmatrix} = \frac{1}{E} \begin{bmatrix} 1 & -\nu & -\nu & 0 & 0 & 0 \\ & 1 & -\nu & 0 & 0 & 0 \\ & & 1 & 0 & 0 & 0 \\ & & & 2(1+\nu) & 0 & 0 \\ & & & & 2(1+\nu) & 0 \\ \text{symm} & & & & & 2(1+\nu) \end{bmatrix} \begin{bmatrix} \sigma_{11} \\ \sigma_{22} \\ \sigma_{33} \\ \sigma_{23} \\ \sigma_{13} \\ \sigma_{12} \end{bmatrix}$$

Invert

$$\begin{bmatrix} \sigma_{11} \\ \sigma_{22} \\ \sigma_{33} \\ \sigma_{23} \\ \sigma_{13} \\ \sigma_{12} \end{bmatrix} = \begin{bmatrix} \lambda+2\mu & \lambda & \lambda & 0 & 0 & 0 \\ & \lambda+2\mu & \lambda & 0 & 0 & 0 \\ & & \lambda+2\mu & 0 & 0 & 0 \\ & & & \mu & 0 & 0 \\ & & & & \mu & 0 \\ \text{symm} & & & & & \mu \end{bmatrix} \begin{bmatrix} \varepsilon_{11} \\ \varepsilon_{22} \\ \varepsilon_{33} \\ 2\varepsilon_{23} \\ 2\varepsilon_{13} \\ 2\varepsilon_{12} \end{bmatrix}$$

Here, λ and μ are the Lamé parameters

$$\lambda = \frac{E\nu}{(1+\nu)(1-2\nu)}, \mu = G = \frac{E}{2(1+\nu)} \tag{6}$$

For simplicity, the generalized Hooke's law can be described as the linear relation among all the components of the stress and strain tensor

$$\sigma_{ij} = C_{ijkl}\varepsilon_{kl} \tag{7}$$

where C_{ijkl} are the components of the fourth-order stiffness tensor of the elastic moduli.

The stiffness tensor has the following minor symmetries, which result from the symmetry of the stress and strain tensors

$$\sigma_{ij} = \sigma_{ji}$$

$$C_{jikl} = C_{ijkl} \tag{8}$$

Such as the matrix above.

$\sigma_{ij} = C_{ijkl}\varepsilon_{kl}$ represents

$$\begin{bmatrix} \sigma_{11} \\ \sigma_{22} \\ \sigma_{33} \\ \sigma_{23} \\ \sigma_{13} \\ \sigma_{12} \end{bmatrix} = \begin{bmatrix} C_{1111} & C_{1122} & C_{1133} & 0 & 0 & 0 \\ & C_{2222} & C_{2323} & 0 & 0 & 0 \\ & & C_{3333} & 0 & 0 & 0 \\ & & & C_{2323} & 0 & 0 \\ & & & & C_{1313} & 0 \\ \text{symm} & & & & & C_{1212} \end{bmatrix} \begin{bmatrix} \varepsilon_{11} \\ \varepsilon_{22} \\ \varepsilon_{33} \\ 2\varepsilon_{23} \\ 2\varepsilon_{13} \\ 2\varepsilon_{12} \end{bmatrix}$$

For thermoelastic effects

$$\varepsilon_{ij}^{T} = \alpha\Delta T\delta_{ij} \tag{9}$$

where ε_{ij}^{T} is the thermal strain, α is the thermal expansion coefficient, and δ_{ij} is the Kronecker delta.

The total strains are those produced by the mechanical strains and the thermal strains

$$\varepsilon_{ij} = \varepsilon_{ij}^{M} + \varepsilon_{ij}^{T}$$

$$\sigma_{ij} = C_{ijkl}(\varepsilon_{kl} - \alpha\Delta T\delta_{kl}) \tag{10}$$

When the thermal effects are considered, the relationship between stress and strain is given by

$$\sigma_{ij} = C_{ijkl}(\varepsilon_{kl} - \alpha\Delta T\delta_{kl}) \tag{11}$$

Here, the macro was continued to create nodes and FEs. The model with dimensions of 35 mm by 10 mm by 20 μm was used for the PC membrane part, and the model with dimensions of 10 mm by 10 mm by 5 μm was used for the MXCC part and partly embedded in the center of SOLID45 element. Hexahedral meshes were generated across the whole actuator, and more segmentation hexahedral meshes were generated on the MXCC part according to the specifics of the design (fig. S10). Displacement and symmetrical constrains were also implemented for the boundary conditions in the FE model. Uniformed loading and the torque versus *y* axis were applied to the actuator.

SUPPLEMENTARY MATERIALS

Supplementary material for this article is available at http://advances.sciencemag.org/cgi/content/full/5/7/eaaw7956/DC1

Fig. S1. The structure and composition of MXene, cellulose, and composites.
Fig. S2. The microstructure and morphology of the cellulose film and MXene.
Fig. S3. The MXCC ink and a typical MXCC/PC bilayer-structured actuator.
Fig. S4. The humidity-responsive capability of the MXCC/PC bilayer-structured actuator.
Fig. S5. The electricity-responsive capability of the MXCC/PC bilayer-structured actuator.
Fig. S6. The NIR light-responsive capability of the MXene based actuator.
Fig. S7. Weight changes as a function of time during light turned on (5 s) and off (600 s) for an MXCC/PDMS bilayer-structured actuator.
Fig. S8. The experimental setup for measuring static force and strain and cycle performance of the MXCC/PC bilayer-structured actuator.
Fig. S9. Simulation model of the MXCC-based actuator.
Fig. S10. NIR light responsiveness of the double folding actuator and the load-lifting capacity of the MXCC-based actuator.
Note S1. Calculations of the energy density and power density of our MXCC-based actuator.
Movie S1. A real-time digital camera video of the MXCC/PC bilayer-structured actuator upon sequential on/off NIR light irradiation (illumination intensity, 80 mW cm^{-2}).
Movie S2. A real-time IR camera video of the MXCC/PC bilayer-structured actuator upon sequential on/off NIR light irradiation (illumination intensity, 80 mW cm^{-2}).
Movie S3. Simulated actuation process of the MXCC-based actuator.
Movie S4. A real-time digital camera video of self-folding box upon sequential on/off NIR light irradiation.
Movie S5. A real-time digital camera video of self-blooming flower upon sequential on/off NIR light irradiation.
Movie S6. A real-time digital camera video of worm-like robot upon sequential on/off NIR light irradiation.
Movie S7. A real-time digital camera video of smart switch upon sequential on/off NIR light irradiation.
Movie S8. A real-time IR camera video of a butterfly silhouette–shaped MXCC device upon sequential on/off NIR light irradiation.
Reference (*43*)

REFERENCES AND NOTES

1. M. Ma, L. Guo, D. G. Anderson, R. Langer, Bio-inspired polymer composite actuator and generator driven by water gradients. *Science* **339**, 186–189 (2013).
2. L. Chen, M. Weng, Z. Zhou, Y. Zhou, L. Zhang, J. Li, Z. Huang, W. Zhang, C. Liu, S. Fan, Large-deformation curling actuators based on carbon nanotube composite: Advanced-structure design and biomimetic application. *ACS Nano* **9**, 12189–12196 (2015).

3. X. Zhang, Z. Yu, C. Wang, D. Zarrouk, J.-W. T. Seo, J. C. Cheng, A. D. Buchan, K. Takei, Y. Zhao, J. W. Ager, J. Zhang, M. Hettick, M. C. Hersam, A. P. Pisano, R. S. Fearing, A. Javey, Photoactuators and motors based on carbon nanotubes with selective chirality distributions. *Nat. Commun.* **5**, 2983 (2014).
4. Q. Li, C. Liu, Y.-H. Lin, L. Liu, K. Jiang, S. Fan, Large-strain, multiform movements from designable electrothermal actuators based on large highly anisotropic carbon nanotube sheets. *ACS Nano* **9**, 409–418 (2015).
5. D.-D. Han, Y.-L. Zhang, H.-B. Jiang, H. Xia, J. Feng, Q.-D. Chen, H.-L. Xu, H.-B. Sun, Moisture-responsive graphene paper prepared by self-controlled photoreduction. *Adv. Mater.* **27**, 332–338 (2015).
6. C. Ma, W. Lu, X. Yang, J. He, X. Le, L. Wang, J. Zhang, M. J. Serpe, Y. Huang, T. Chen, Bioinspired anisotropic hydrogel actuators with on–off switchable and color-tunable fluorescence behaviors. *Adv. Funct. Mater.* **28**, 1704568 (2018).
7. Q. Zhao, W. Zou, Y. Luo, T. Xie, Shape memory polymer network with thermally distinct elasticity and plasticity. *Sci. Adv.* **2**, e1501297 (2016).
8. W.-E. Lee, Y.-J. Jin, L.-S. Park, G. Kwak, Fluorescent actuator based on microporous conjugated polymer with intramolecular stack structure. *Adv. Mater.* **24**, 5604–5609 (2012).
9. X. Lu, H. Zhang, G. Fei, B. Yu, X. Tong, H. Xia, Y. Zhao, Liquid-crystalline dynamic networks doped with gold nanorods showing enhanced photocontrol of actuation. *Adv. Mater.* **30**, 1706597 (2018).
10. D. Van Opdenbosch, G. Fritz-Popovski, W. Wagermaier, O. Paris, C. Zollfrank, Moisture-driven ceramic bilayer actuators from a biotemplating approach. *Adv. Mater.* **28**, 5235–5240 (2016).
11. R. Kainuma, Y. Imano, W. Ito, Y. Sutou, H. Morito, S. Okamoto, O. Kitakami, K. Oikawa, A. Fujita, T. Kanomata, K. Ishida, Magnetic-field-induced shape recovery by reverse phase transformation. *Nature* **439**, 957–960 (2006).
12. H. Arazoe, D. Miyajima, K. Akaike, F. Araoka, E. Sato, T. Hikima, M. Kawamoto, T. Aida, An autonomous actuator driven by fluctuations in ambient humidity. *Nat. Mater.* **15**, 1084–1089 (2016).
13. X. Zhang, C. L. Pint, M. H. Lee, B. E. Schubert, A. Jamshidi, K. Takei, H. Ko, A. Gillies, R. Bardhan, J. J. Urban, M. Wu, R. Fearing, A. Javey, Optically- and thermally-responsive programmable materials based on carbon nanotube-hydrogel polymer composites. *Nano Lett.* **11**, 3239–3244 (2011).
14. C. Xu, G. T. Stiubianu, A. A. Gorodetsky, Adaptive infrared-reflecting systems inspired by cephalopods. *Science* **359**, 1495–1500 (2018).
15. H. Ying, J. Liu, L. Chang, L. Yang, A. Xu, K. Qi, P. Lu, G. Wu, W. Chen, Y. Wu, Electrically and sunlight-driven actuator with versatile biomimetic motions based on rolled carbon nanotube bilayer composite. *Adv. Funct. Mater.* **27**, 1704388 (2017).
16. P. Chen, Y. Xu, S. He, X. Sun, S. Pan, J. Deng, D. Chen, H. Peng, Hierarchically arranged helical fibre actuators driven by solvents and vapours. *Nat. Nanotechnol.* **10**, 1077–1083 (2015).
17. J. F. Mano, Stimuli-responsive polymeric systems for biomedical applications. *Adv. Eng. Mater.* **10**, 515–527 (2008).
18. S. A. Morin, R. F. Shepherd, S. W. Kwok, A. A. Stokes, A. Nemiroski, G. M. Whitesides, Camouflage and display for soft machines. *Science* **337**, 828–832 (2012).
19. L. Chen, M. Weng, P. Zhou, L. Zhang, Z. Huang, W. Zhang, Multi-responsive actuators based on a graphene oxide composite: Intelligent robot and bioinspired applications. *Nanoscale* **9**, 9825–9833 (2017).
20. R. H. Baughman, Conducting polymer artificial muscles. *Synth. Met.* **78**, 339–353 (1996).
21. S. Maeda, Y. Hara, T. Sakai, R. Yoshida, S. Hashimoto, Self-walking gel. *Adv. Mater.* **19**, 3480–3484 (2007).
22. A. Villanueva, C. Smith, S. Priya, A biomimetic robotic jellyfish (Robojelly) actuated by shape memory alloy composite actuators. *Bioinspir. Biomim.* **6**, 036004 (2011).
23. J. Chen, G. Liu, J. Cheng, S. Dong, Actuation performance and heat generation of shear-bending actuator based on $BiScO_3$-$PbTiO_3$ ceramics from 25 to 300 °C. *Appl. Phys. Lett.* **107**, 032906 (2015).
24. Y. Xia, T. S. Mathis, M.-Q. Zhao, B. Anasori, A. Dang, Z. Zhou, H. Cho, Y. Gogotsi, S. Yang, Thickness-independent capacitance of vertically aligned liquid-crystalline MXenes. *Nature* **557**, 409–412 (2018).
25. Z. Ling, C. E. Ren, M.-Q. Zhao, J. Yang, J. M. Giammarco, J. Qiu, M. W. Barsoum, Y. Gogotsi, Flexible and conductive MXene films and nanocomposites with high capacitance. *Proc. Natl. Acad. Sci. U.S.A.* **111**, 16676–16681 (2014).
26. R. Liu, W. Li, High-thermal-stability and high-thermal-conductivity $Ti_3C_2T_x$ MXene/Poly (vinyl alcohol) (PVA) composites. *ACS Omega* **3**, 2609–2617 (2018).
27. R. Li, L. Zhang, L. Shi, P. Wang, MXene Ti_3C_2: An effective 2D light-to-heat conversion material. *ACS Nano* **11**, 3752–3759 (2017).
28. J. Come, J. M. Black, M. R. Lukatskaya, M. Naguib, M. Beidaghi, A. J. Rondinone, S. V. Kalinin, D. J. Wesolowski, Y. Gogotsi, N. Balke, Controlling the actuation properties of MXene paper electrodes upon cation intercalation. *Nano Energy* **17**, 27–35 (2015).
29. G. G. Coté, Diversity and distribution of idioblasts producing calcium oxalate crystals in *Dieffenbachia seguine* (Araceae). *Am. J. Bot.* **96**, 1245–1254 (2009).
30. H. Zhou, X. Li, T. Fan, F. E. Osterloh, J. Ding, E. M. Sabio, D. Zhang, Q. Guo, Artificial inorganic leafs for efficient photochemical hydrogen production inspired by natural photosynthesis. *Adv. Mater.* **22**, 951–956 (2010).
31. H. Lin, X. Wang, L. Yu, Y. Chen, J. Shi, Two-dimensional ultrathin MXene ceramic nanosheets for photothermal conversion. *Nano Lett.* **17**, 384–391 (2016).
32. C. Lv, X.-C. Sun, H. Xia, Y.-H. Yu, G. Wang, X.-W. Cao, S.-X. Li, Y.-S. Wang, Q.-D. Chen, Y.-D. Yu, H.-B. Sun, Humidity-responsive actuation of programmable hydrogel microstructures based on 3D printing. *Sens. Actuat. B Chem.* **259**, 736–744 (2018).
33. M. Amjadi, M. Sitti, High-performance multiresponsive paper actuators. *ACS Nano* **10**, 10202–10210 (2016).
34. E. Sachyani, M. Layani, G. Tibi, T. Avidan, A. Degani, S. Magdassi, Enhanced movement of CNT-based actuators by a three-layered structure with controlled resistivity. *Sens. Actuat. B Chem.* **252**, 1071–1077 (2017).
35. Z. Chen, R. Cao, S. Ye, Y. Ge, Y. Tu, X. Yang, Graphene oxide/poly (*N*-isopropylacrylamide) hybrid film-based near-infrared light-driven bilayer actuators with shape memory effect. *Sens. Actuat. B Chem.* **255**, 2971–2978 (2018).
36. J. Mu, C. Hou, H. Wang, Y. Li, Q. Zhang, M. Zhu, Origami-inspired active graphene-based paper for programmable instant self-folding walking devices. *Sci. Adv.* **1**, e1500533 (2015).
37. W. Wang, C. Xiang, Q. Zhu, W. Zhong, M. Li, K. Yan, D. Wang, Multistimulus responsive actuator with GO and carbon nanotube/PDMS bilayer structure for flexible and smart devices. *ACS Appl. Mater. Interfaces* **10**, 27215–27223 (2018).
38. T. Messin, N. Follain, A. Guinault, G. Miquelard-Garnier, C. Sollogoub, N. Delpouve, V. Gaucher, S. Marais, Confinement effect in PC/MXD6 multilayer films: Impact of the microlayered structure on water and gas barrier properties. *J. Membr. Sci.* **525**, 135–145 (2017).
39. Q. Zhao, J. W. C. Dunlop, X. Qiu, F. Huang, Z. Zhang, J. Heyda, J. Dzubiella, M. Antonietti, J. Yuan, An instant multi-responsive porous polymer actuator driven by solvent molecule sorption. *Nat. Commun.* **5**, 4293 (2014).
40. R. H. Baughman, Materials Science: Playing nature's game with artificial muscles. *Science* **308**, 63–65 (2005).
41. I. S. Romero, N. P. Bradshaw, J. D. Larson, S. Y. Severt, S. J. Roberts, M. L. Schiller, J. M. Leger, A. R. Murphy, Biocompatible electromechanical actuators composed of silk-conducting polymer composites. *Adv. Funct. Mater.* **24**, 3866–3873 (2014).
42. M. Alhabeb, K. Maleski, B. Anasori, P. Lelyukh, L. Clark, S. Sin, Y. Gogotsi, Guidelines for synthesis and processing of two-dimensional titanium carbide ($Ti_3C_2T_x$ MXene). *Chem. Mater.* **29**, 7633–7644 (2017).
43. R. A. Khan, S. Salmieri, D. Dussault, J. Uribe-Calderon, M. R. Kamal, A. Safrany, M. Lacroix, Production and properties of nanocellulose-reinforced methylcellulose-based biodegradable films. *J. Agric. Food Chem.* **58**, 7878–7885 (2010).

Acknowledgments: We appreciate W. Liu and P. Buenconsejo [Facility for Analysis Characterisation Testing and Simulation (FACTS), Nanyang Technological University] for the in situ XRD measurements, and we appreciate X. Zhou, P. Cui, D. Gao, Y. Mai, J. Wang, and J. Chen for the helpful discussion. **Funding:** We gratefully acknowledge funding from the Competitive Research Programme under NRF-CRP-13-2014-02; NRF Investigatorship under NRF-NRFI2016-05; and the Campus for Research Excellence and Technological Enterprise (CREATE) programme under the National Research Foundation, Prime Minister's Office, Singapore. **Author contributions:** P.S.L. proposed the research direction and guided the project. G.C. designed and performed the fabrication and characterization of the actuator system. J.-H.C. performed synthesis and characterization of the MXene material and the photothermal conversion performance of the actuator system. Y.L. performed computer simulations. Y.J. performed mechanical property measurements. G.C. and P.S.L. were the primary writers of the manuscript. All authors discussed the results and provided feedback on the manuscript. **Competing interests:** The authors declare that they have no competing interests. **Data and materials availability:** All data needed to evaluate the conclusions in the paper are present in the paper and/or the Supplementary Materials. Additional data related to this paper may be requested from the authors.

Submitted 25 January 2019
Accepted 6 June 2019
Published 12 July 2019
10.1126/sciadv.aaw7956

Citation: G. Cai, J.-H. Ciou, Y. Liu, Y. Jiang, P. S. Lee, Leaf-inspired multiresponsive MXene-based actuator for programmable smart devices. *Sci. Adv.* **5**, eaaw7956 (2019).